

# Measuring the evolution of early-type galaxies in GAMA using observationally robust quantities

Rongfu Liu, Alessandro Sonnenfeld

Accepted XXX. Received YYY; in original form ZZZ

## ABSTRACT

Quiescent galaxies today is believed to have experienced more dramatic growth in their evolution history, comparing their star-forming counterpart. Traditionally, most of the method used to investigate the evolution of these object involved the total light of one galaxy, which we believed to be not well-defined and is likely to suffer from extrapolation problem. In this work, we use a different parameterization, namely  $M_{*,10}$  and  $\Gamma_{*,10}$  which is the mass and the mass-weighted density slope enclosed in circularised aperture 10kpc respectively, to provide a new perspective. We first analyses a collection of binary-merger simulations and find that the growth in  $M_{*,10}$  and  $\Gamma_{*,10}$  are different in different merger scenarios and different galaxies size. We then select a  $M_{*,10}$  complete sample of galaxies in GAMA survey and use KiDs r-band image to provide structural parameters. We measured  $M_{*,10}$  and  $\Gamma_{*,10}$  for these galaxies, and compare the evolutionary trend with simulation results. We find that for galaxies with  $M_{*,10} \geq 10^{10.9} M_\odot$  and redshift  $0.15 \leq z \leq 0.40$ , no significant evidence shows they experienced a growth due to merger of any kinds.

**Key words:** keyword1 – keyword2 – keyword3

## 1 INTRODUCTION

Early type galaxies (ETGs), which are typically elliptical in shape, are believed to have complete most of their star-forming activities before the epoch of  $z \approx 2$  and are passively evolved afterwards. Besides the focus on what mechanism that shut down the star formation, the passive evolving process of these galaxies is also a highly debated subjects in the field of galaxy evolution. Obtaining a better understanding on this process could help us better understand the hierarchical structure formation theory, which is a fundamental theory in  $\Lambda$ CDM cosmology.

Over the past few decades, observations have suggested that quenched ETGs are much more compact than their counterpart at  $z \approx 0$  (Daddi et al. 2005; Toft et al. 2007; Trujillo et al. 2006, 2007; van Dokkum et al. 2008). As a consequence, the passive evolution process of the quiescent, ultra-compact objects experienced are believed to have induced a dramatic growth in size, in particular, by about a factor of 3 between  $z = 2$  and  $z = 0$  (Damjanov et al. 2019; Fan et al. 2008; Hamadouche et al. 2022; van der Wel et al. 2014; van Dokkum et al. 2010). Given that the star formation rate of these ETGs are relatively low, van Dokkum et al. (2010) suggested that the these galaxies should have experienced a built-up process of their outer envelope since  $z \approx 1.5$  via some form of merging and accretion. Numerous works in literature that based on both observations and hydrodynamic simulations have suggested that the dissipationless dry mergers might be the major growth mechanism, as it could explain the evolution in size, density profile, central densities and orbital structures of these quiescent galaxies (Naab et al. 2009; van Dokkum & Brammer 2010; Oser et al. 2011; Newman et al. 2012; Hilz et al. 2013; Dekel & Burkert 2014; D'Eugenio et al. 2023). In particular, minor mergers, which means the mass ratio between the accreted galaxy and the progenitor galaxy is relatively small, are be-

lieved to have dominated the merger event that one galaxy might experience, especially for mergers with mass ratio around 1:10 (Newman et al. 2012; Belli et al. 2015). Taking the advantage of the depth and resolution of JWST Advanced Deep Extragalactic Survey (Gardner et al. 2023; Eisenstein et al. 2023), we are enabled to detect very low mass ratio ( $\leq 1 : 100$ )mergers. The result also suggest that mergers with ratio close to 1:10 are likely to drive the size growth while lower mass ratio mergers might dominate the color gradients evolution (Suess et al. 2023).

However, although minor merger scenario has made a great success in explaining the evolution of ETGs, there's still some issues that has not been solved. For instance, at redshift  $z \geq 1$ , minor mergers alone seems insufficient. Both observations and prediction seems to suggested a more rapid growth rate due to the accretion with satellite galaxies, comparing to the predicted value we made with the assumption that all the accreted mass are from minor mergers (Hopkins et al. 2010; Nipoti et al. 2009). The evolution in the density slope of galaxies in this minor merger scenario might also not be consistent with observations (Sonnenfeld et al. 2014). While at intermediate redshift, a mass-dependent growth rate is suggested, but the result seems less conclusive. van der Wel et al. (2014); Roy et al. (2018) found out that the massive ETGs ( $M_* \geq 10^{11} M_\odot$ )are likely to grows most rapid in size, comparing to less massive counterparts. While Damjanov et al. (2019) suggest a contrast trend, she found the size growth of massive quiescent galaxies are significantly slower than that of less massive ones. She suggested that mechanism that drives the size growth may have altered in this intermediate redshift range, thus detailed observation should pay more attention to that epoch. In fact, taking the result from Bundy et al. (2017) into consideration, which do not suggest a significant growth in number density of massive ETGs during  $0.3 < z < 0.65$ , we cannot conclude for sure if and how that quiescent galaxies grow at this intermediate redshift range.

To further investigate this issue, we also need to deal with the systematics carefully. The existence of systematics would limit our ability to measure the growth of ETGs precisely. Among various systematics, the progenitor bias is one that commonly addressed in literature. The population of quiescent galaxies are not static, star-forming galaxies could be quenched and join the quiescent population continuously. If these "fresh bloods" are relatively larger, the change in demography could thus mimic the evolution in average size that minor merger process may induce (Dokkum & Franx 1996; Carollo et al. 2013; Fagioli et al. 2016; van Dokkum & Franx 2001). In fact, our understanding about the growth of quiescent galaxies could still be improved, a detailed theoretical model that could take some additional minor mechanisms (e.g. major mergers) and possible systematic (e.g. progenitor bias) into account is still in absence.

Besides, another possible systematic might be ignored in the literature. The problem arise from the finite photometric depth of observations. It is hard to measure the total light directly (Tal & van Dokkum 2011) as the information where the surface brightness of galaxies drops below the observation limit remains unknown. To obtain a accurate measurement of the total light, a precise sky-subtraction is demanded, while it is easy to bring additional systematic. In literature, we use various models to fit the surface brightness distribution of galaxies. The faint outskirt of galaxies could not provide reliable constrains during the fitting process, thus the model could not be able to provide reliable descriptions for surface brightness there. These unreliable data will be accounted in the total light measurement and will take up an ineligible fraction (Sonnenfeld 2020). However, the traditional definition of galaxy size and mass derived from the best-fit model are both associated with the total light, therefore we believe they are not robust qualities.

One of the main goal of this work is to eliminate the possible bias that introduced by the data measured in the unreliable outer region of galaxies. In particular, we switch our focus from the entire galaxy to a fixed, relatively small aperture following the method proposed in Sonnenfeld (2020). In this work, we choose 10kpc as that aperture, in consideration that it is large enough to enclose sufficient amount of stellar mass while will not be too large to suffer from the extrapolation problem. We use  $M_{*,10}$  to denote the mass enclosed inside 10kpc and  $\Gamma_{*,10}$  to represent to mass-weighted projected surface density slope. The latter is defined as

$$\Gamma_{*,10} = \frac{2\pi \int_0^{10} R \frac{d\log \Sigma_*}{d\log R} \Sigma_*(R) dR}{2\pi \int_0^{10} R \Sigma_*(R) dR} = 2 - \frac{2\pi \times 10^2 \times \Sigma_*(10)}{M_{*,10}} \quad (1)$$

We replace the traditional definition of galaxy size (effective radius  $R_e$ ) and stellar mass ( $M_*$ ) with these two quantities, thus the relation between  $M_{*,10}$  and  $\Gamma_{*,10}$  could provide a new insight into the traditional scaling relation. With the help of these new robust quantities, we hope to answer the following questions:

1. Whether quiescent galaxies grow in a given redshift range?
2. If galaxies do growth, what could be the possible mechanisms that drive the growth?

Therefore, it's necessary to understand the impact of various growth mechanism, in particular, mergers with different merger ratio. Assuming a isothermal density profile for elliptical galaxy, the growth in total stellar mass and effective radius due to mergers can be approximated by some simple formulas using virial theorem (Naab et al. 2009). However, switching to  $M_{*,10}$  and  $\Gamma_{*,10}$  space, it's hard to derive a relation in  $\Delta M_{*,10}$  and  $\Delta \Gamma_{*,10}$  analytically as a fixed aperture size 10kpc is involved. Nevertheless, N-body simulations can be helpful. We utilize the simulation result from Nipoti et al. (2009)

which contains a number of binary mergers with different mass ratio. We measure the  $M_{*,10}$  and  $\Gamma_{*,10}$  of both progenitor and merger remnant and calculate the growth in these two quantities. In addition to finding that different merger ratio behaves differently, we also discovered that the scale of galaxy also make differences.

Having find how the  $M_{*,10}$  and  $\Gamma_{*,10}$  under different growth scenarios, we then compared them with the evolution of these two quantities in reality. We select ETGs from GAMA DR4 main survey (Galaxy and Mass Assembly, Driver et al. (2022); Bellstedt et al. (2020); Baldry et al. (2010); Hopkins et al. (2013)) and obtained precise spectroscopic redshift and other quantities that related to spectrum measurement, e.g. stellar mass. In addition, the structural parameter are measured from KiDs photometry (Kile Degree survey, Kuijken et al. (2019), Roy et al. (2018), Amaro et al. (2021)) using GalNet (Li et al. (2022)). Based on these observation datas, we then calculated their  $M_{*,10}$  and  $\Gamma_{*,10}$  and further analyse the  $M_{*,10} - \Gamma_{*,10}$  relation and their evolution from  $z = 0.6$  to present.

The structure of this paper is as follows. In Sect.1, we give a brief description on both observations from KiDs&GAMA and the binary merger simulation from (Nipoti et al. 2009). We present the result of growth of  $M_{*,10}$  and  $M_{*,10} - \Gamma_{*,10}$  in different merger scenarios in Sect.3 and present the comparison with observation result in Sect.4. Finally, We give a discussion in Sect.5 then conclude the paper in Sect.6.

In this paper, we assume a flat  $\Lambda$ CDM cosmology with  $\Omega_M = 0.3$  and  $H_0 = 70 \text{ km s}^{-1} \text{ Mpc}^{-1}$ . Magnitude are in AB units and stellar mass are in solar units.

## 2 OBSERVATION

### 2.1 Sample selection

Our goal of this work is to focus on the evolution of quiescent galaxies at intermediate redshift range and attempting to elliminate a possible systematic from the extrapolation problem by focusing on a fixed aperture size 10kpc. We expect to select a sample that consist of quiescent galaxies with spectroscopic data, hence obtain reliable measurement of redshift, stellar mass, aperture size and could distinguish them from star-forming ones. In addition, as our requirement of focusing the inner region, we need to obtain the structural parameters of galaxies in order to calculate  $M_{*,10}$  and  $\Gamma_{*,10}$ .

Therefore, we choose to select galaxies based on GAMA DR4. In practice, We use DMU gkvScienceCatv02 (Bellstedt et al. (2020)) to select galaxies from GAMA DR4 Main Survey sample, which covers  $230.2 \text{ deg}^2$  region and only include galaxies whose r-band magnitude is larger than 19.65 in order to ensure the 95% spec-z completeness of the sample. Further, We obtain the intensity of emission lines from DMU GaussFitSimplev05 (see Gordon et al. (2017)) and obtain the stellar mass measurement from DMU StellarMassesGKVv24 (see Driver et al. (2022)). According to Taylor et al. (2011), estimation of stellar mass was done by fitting the Bruzual & Charlot (2003) stellar evolution models with Chabrier (2003) stellar initial mass function (IMF) and the Calzetti et al. (2000) dust curve. In particular, the SEDs was weighted to ensure the model-fitting was operated within a fixed wavelength range (3000 - 11000Å).

In order to select ETGs, we use a spectroscopic index  $D_n4000$  to distinguish the quiescent galaxies. In GAMA, this index is defined using the narrow band definition of Balogh et al. (1999), which is the ratio between the flux per unit frequency in 4000 - 4100Å and 3850 - 3950Å. This index is commonly used as a indicator of the age of stellar population. In this work, we utilize the nature that the

distribution of  $D_n$ 4000 index exhibit a strong bimodality. According to [Kauffmann et al. \(2003\)](#), the distribution shows a clear division between star-forming and quiescent galaxies at  $D_n$ 4000 = 1.5, hence we adopt this division as our selection criteria for quiescent galaxies. In addition, We removed galaxies whose normalized redshift quality  $nQ < 2$  following the suggestion by GAMA Collaboration([Driver et al. 2022](#)).

In addition, we exclude galaxies that are not overlapped with KiDs([Kuijken et al. \(2019\)](#)), in order to utilize the measurement of structural parameters based on KiDs image. The structural parameter are measured by GalNet([Li et al. \(2022\)](#)), which has operated a single Sérsic model fitting to the surface brightness of KiDs DR5 galaxies(RUILI IN PREPARATION) using its r-band photometry. We further exclude some galaxies with catastrophic measurement which gives ridiculous values of effective radius or stellar mass. Eventually we have 79672 ETGs with measurement of spectroscopic redshift, stellar mass and structural parameters.

## 2.2 $M_{*,10}, \Gamma_{*,10}$ measurement

As is mentioned above, we do not trust  $M_*$  (total stellar mass) and  $R_e$  (effective radius) in traditional structural parameters as they are related with the unreliable data in the faint outer region of a galaxies, which can only be obtained by extrapolate the surface brightness model. Consequently, we use a new set of parameters:  $M_{*,10}$  and  $\Gamma_{*,10}$  as replacement and focus on their relation and the evolution of such relation. In this work, we use Sérsic profile to model the surface brightness of galaxies, then calculate  $M_{*,10}$  and  $\Gamma_{*,10}$  using the Sérsic parameters, although it seems ridiculous as such procedure still involved using  $M_*$  and  $R_e$  which we claimed unreliable. In fact, we believe that best-fitting model is well-constrained by the inner region, and thus it is reasonable to use them describing the shape of the surface brightness profile there, in particular,  $10\text{kpc}$ .

The Sérsic profile can be described by:

$$I(R) = I_0 \exp \left\{ -b_n \left( \frac{R}{R_e} \right)^{1/n} \right\} \quad (2)$$

Here,  $q$  is the axis ratio,  $n$  is the Sérsic index while  $R$  is the circularised radius

$$R^2 = qx^2 + \frac{y^2}{q} \quad (3)$$

where  $x, y$  are Cartesian coordinates, located at the center of galaxies. We use symbol  $x$  to denote the axis that is aligned with the semi-major axis of the ellipse, while using  $y$  to denote axis aligned with semi-minor axis. The effective radius  $R_e$  is circularised as well.

Integrating Eq.2, we can obtain the light enclosed in a certain aperture  $L(< R)$

$$L(< R) = 2\pi n \cdot I_0 R_e^2 \cdot \frac{1}{(b_n)^{2n}} \cdot \gamma \left[ 2n, b_n \left( \frac{R}{R_e} \right)^{\frac{1}{n}} \right] \quad (4)$$

The total light is simply substitute  $R = \infty$  to Eq.4

$$L_{tot} = 2\pi n \cdot I_0 R_e^2 \cdot \frac{1}{(b_n)^{2n}} \cdot \Gamma(2n) \quad (5)$$

Here  $\Gamma$  is the gamma function,  $\gamma$  is the lower incomplete gamma function and  $b_n$  is a constant that ensure the light enclosed within the effective radius  $R_e$  is a half of the total light.

$$L_{tot} = 2L(< R_e) \quad (6)$$

Therefore,  $b_n$  can be calculated by solving

$$\Gamma(2n) = 2\gamma(2n, b_n) \quad (7)$$

In our work, we assume that there is no mass-to-light ratio gradient inside one galaxy, hence the mass profile can be easily obtained via the light profile. We have obtained the stellar mass estimate for each galaxy from GAMA together with the light they use in the SPS model fitting process ([Driver et al. 2022](#)), which enable us to calculate the mass-to-light ratio  $\Upsilon_*$ . The mass profile can be easily obtained by multiplying Eq3 and Eq4 with that  $\Upsilon_*$ .

$$\Sigma_*(R) = \Upsilon_* I_0 \exp \left\{ -b_n \left( \frac{R}{R_e} \right)^{1/n} \right\} \quad (8)$$

$$M_*(< R) = \Upsilon_* 2\pi n \cdot I_0 R_e^2 \cdot \frac{1}{(b_n)^{2n}} \cdot \gamma \left[ 2n, b_n \left( \frac{R}{R_e} \right)^{\frac{1}{n}} \right] \quad (9)$$

Simply substitute  $R = 10\text{kpc}$  to Eq.9, we obtained  $M_{*,10}$ , while  $\Gamma_{*,10}$  is obtained by substituting Eq.8 to Eq.1. In fact, we could only obtain the stellar mass estimation from GAMA survey and structure parameter measurement from KiDs survey. As these two surveys may use different aperture size in investigating the same galaxy, these two quantities might not be consistent. Nevertheless, we may make a assumption that the mass-to-light ratio  $\Upsilon_*$  do not depend on the distance to the center of galaxy. Therefore, although we could only obtain  $\Upsilon_*$  from GAMA survey, we believe it is reasonable to use it to calculate  $M_{*,10}$  and  $\Gamma_{*,10}$  together with the structure parameter measured by KiDs.

Another concern might arise from the fact that galaxies may have various component, hence single Sérsic model might not be able to give a accurate description of the entire surface brightness profile. However, as we are focusing on the inner region of the galaxy, our only requirement is just the surface brightness in the inner region of galaxy can be accurately described by model. We compared the profile of the enclosed light of galaxies with their best-fitting Sérsic model in Fig 1 . We can easily observe that although some model do have discrepancy at some large radii, the enclosed light within  $10\text{kpc}$  is still well constrained by model.

## 2.3 Completeness

To accurately measure the evolution of  $M_{*,10}$  and  $M_{*,10} - \Gamma_{*,10}$  relation, we do not expect any bias be introduced during the sample selection procedure. Therefore, we need our sample to be complete in  $M_{*,10}$ . Our fiducial sample is flux-limited, with its 95% completeness limit down to r-band magnitude 19.65. To obtain a  $M_{*,10}$  complete sample, we need to translate this completeness limit in magnitude to limit in  $M_{*,10}$ .

Then we need to translate the r-band critical magnitude  $r_{crit} = 19.65$  to one critical  $M_{*,10}$ , namely  $M_{*,10}^{crit}$ . In fact, at a given redshift, the ratio between  $M_{*,10}$  and the total flux  $F$  always spread a relatively wide range. Here we made an assumption that the ratio  $M_{*,10}/F$  depend neither on  $M_{*,10}$  nor on  $F$ , meaning that this quantity only describe one overall nature of quiescent galaxies at one given redshift. We then make narrow redshift bins, measure the distribution of  $M_{*,10}/F$  in each bin and find the critical value  $M_{*,10}/F|_{crit}$ , where the cumulative probability reach 95%. Multiplying  $M_{*,10}/F|_{crit}$  by the corresponding flux of  $r_{crit}$ , we obtained the  $M_{*,10}$  limit at that redshift bin.

Fig 2 illustrate the procedure, here we randomly choose three different redshift bins and shows the distribution of  $M_{*,10}/F$  inside,

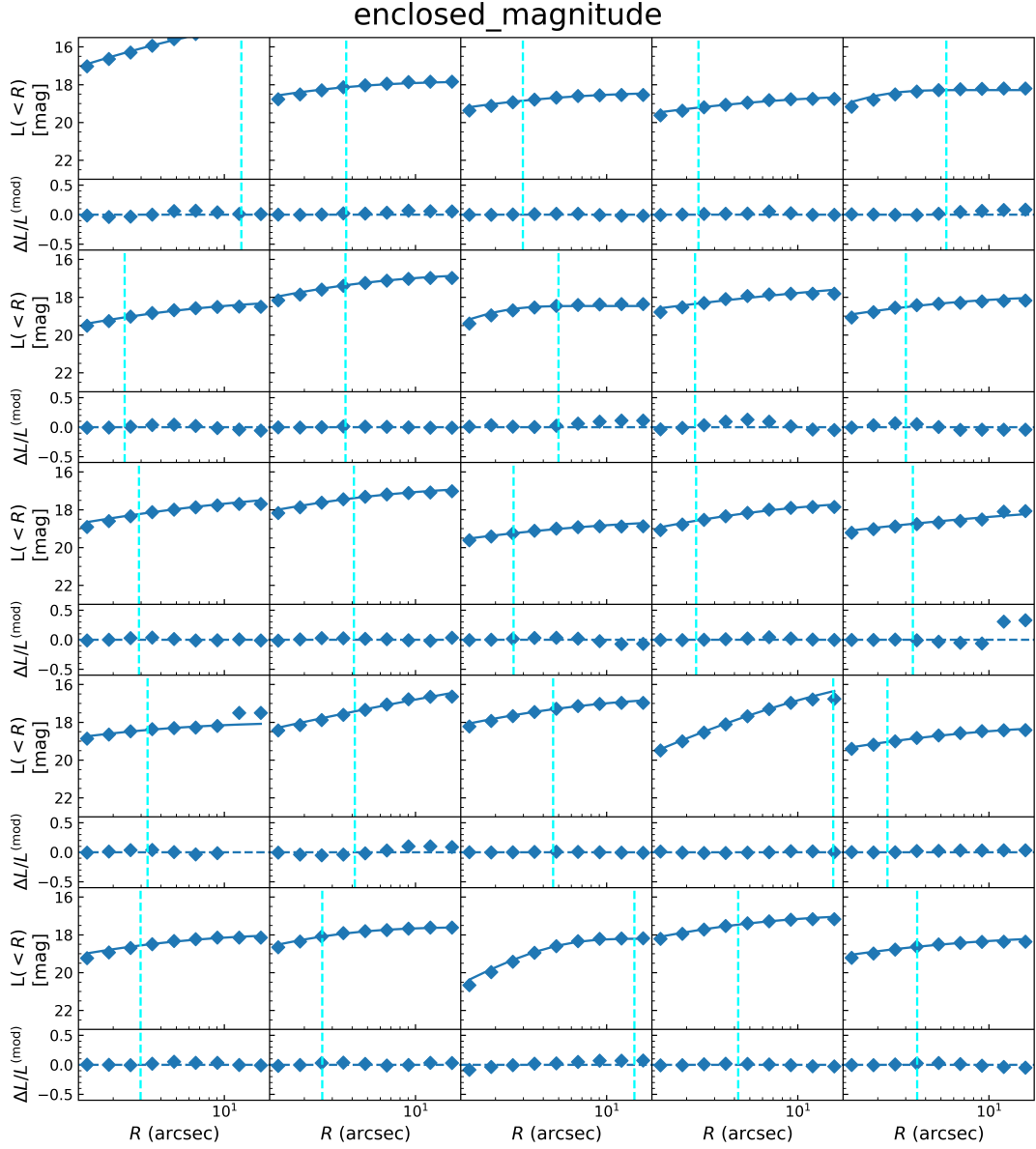


**Figure 1.** The upper panel shows the enclosed magnitude within 10kpc aperture of 25 galaxies that are random selected from our sample. The blue solid line shows the best-fitting Sérsic model calculated using GalNet structural parameters, while the blue diamonds are directly measured from KiDs r-band image. The lower panel shows the difference between the two measurements. The vertical dashed cyan line shows the corresponding angular size of 10kpc of each galaxy.

with dashed line showing the 95% percentile of each bin, i.e. the critical mass-to-flux ratio  $M_{*,10}/F|_{crit}$ . The flux correspond to r-band magnitude 19.65 is  $F_{crit} \approx 5.01 \times 10^{-5}$  Jy. The  $M_{*,10}^{crit}$  in this three bins can thus by  $M_{*,10}^{crit} = M_{*,10}/F|_{crit} \times F_{crit}$  using the value of  $M_{*,10}/F|_{crit}$  in each bins. Operate this procedure iteratively in each redshift bin result in the full 95% completeness limit in  $M_{*,10}$  as a function of redshift  $z$ . In addition, we use a exponential formula to fit this limit

$$f(z) = A(z + B)^C + D \quad (10)$$

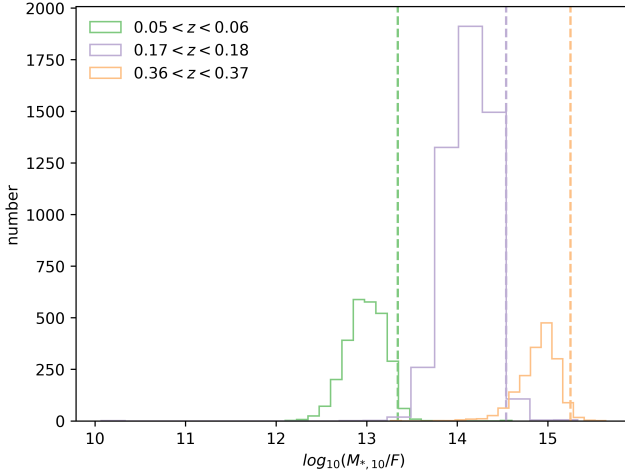
the best-fitting parameter are shown in

Fig 3 shows the distribution of our sample in  $M_{*,10} - z$  space, with the pink solid line shows the 95% completeness limit. We think galaxies whose  $M_{*,10}$  is larger than the limit is 95% possible to be included in our fiducial sample. We thus exclude those galaxies whose

**Table 1.** The best-fitting parameter of the exponential function that describe the 95% completeness limit in  $M_{*,10}$  as a function of redshift.

A	B	C	D
$8.34 \times 10^{-3}$	$9.71 \times 10^{-4}$	$1.06 \times 10^{-4}$	$-8.3 \times 10^{-3}$

$M_{*,10}$  is lower than this limit in our fiducial sample and show these galaxies in grey dots. Galaxies shown in black dots are included to built our complete sample. Actually, we use the galaxies that are shown in cyan dots in this figure to investigate the evolution of  $\Gamma_{*,10}$  and  $M_{*,10} - \Gamma_{*,10}$  relation, as described in Sect.4.2.



**Figure 2.** The distribution of  $M_{*,10}/F$  in three different narrow redshift bins. The vertical dashed line marks the 95% percentile distribution in each bin. Multiply this ratio by the flux corresponding to the r-band magnitude limit  $r_{crit} = 19.65$ , we then obtain the  $M_{*,10}$  limit at that redshift bin.

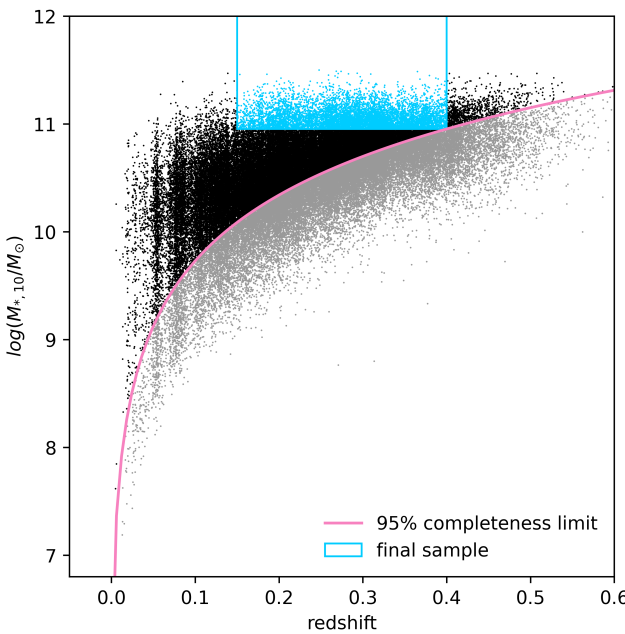


**Figure 3.** 95% completeness  $M_{*,10}$  limit as a function of redshift of our ETG sample, shown in pink solid line. Galaxies above this pink line are adopted in our sample, shown in black dots, and the grey dots that lies below are those being excluded

#### 2.4 $M_{*,10} - \Gamma_{*,10}$ relation

As a consequence of the completeness cut, galaxies with lower  $M_{*,10}$  value at higher redshift would be absent in our sample. To investigate the evolution trend in  $M_{*,10} - \Gamma_{*,10}$  relation, we have to either narrow the redshift range to include more low- $M_{*,10}$  galaxies or narrow the  $M_{*,10}$  range to include more high-redshift galaxies. In this work, we choose the latter one, meaning that we only focus on massive quiescent galaxies whose  $M_{*,10} \geq 10^{10.9} M_\odot$ . In addition, we set a lower

limit on the redshift range  $z \geq 0.15$ . It's easy to observe some vertical stripe-like feature in Fig.3 at low redshift end, and is thought to be the effect of large scale structure by Driver et al. (2022). It is reasonable as the comoving volume at low redshift is relatively smaller, so it is more likely to suffer from cosmic variance. We thus determined this low-redshift cut in order to avoid such cosmic variance. The final sample we used to investigate the evolution is show by cyan dots in Fig.3. We further separate the sample into four different redshift bins.

In order to infer the distribution of  $\Gamma_{*,10}$  as a function of  $M_{*,10}$  in different redshift bins, we use a Bayesian hierarchical method to do the fitting. Each galaxy included in our sample can be described by a set of quantities  $\{\log M_{*,10}, \Gamma_{*,10}, z\}$ . The true value of these quantities, hereafter represented by  $\Theta$ , are drawn from a probability distribution that correlated with the observed data  $\mathbf{d} = \{\log M_{*,10}^{obs}, \Gamma_{*,10}^{obs}, z^{obs}\}$ , and is in turn described by a set of hyperparameters  $\Phi$ . We expect to obtain the posterior distribution of the hyperparameters  $\Phi$  given the observed data  $\mathbf{d}$ :

$$P(\Phi|\mathbf{d}) \propto P(\Phi)P(\mathbf{d}|\Phi) \quad (11)$$

thus we marginalize every possible value of  $\Theta$  in the likelihood part:

$$P(\mathbf{d}|\Phi) = \int P(\mathbf{d}|\Theta)P(\Theta|\Phi)d\Theta \quad (12)$$

As we hope to acquire the  $\Gamma_{*,10} - M_{*,10}$  relation, we may rewrite the second part on the R.H.S. of Eq.12 as

$$P(\Theta|\Phi) = P(\log M_{*,10}|\Phi)P(\Gamma_{*,10}|\Phi, \log M_{*,10}) \quad (13)$$

Note that we have binned the sample into four different redshift bins, hence we ignore the redshift dependence of the hyperparameters  $\Phi$ .

For the distribution of  $\log M_{*,10}$ , we use a skew normal distribution to describe :

$$P(\log M_{*,10}|\Phi) = \frac{1}{\sqrt{2\pi\sigma_M^2}} \exp \left\{ -\frac{(\log M_{*,10} - \mu_M)^2}{2\sigma_M^2} \right\} \mathcal{E}(\log M_{*,10}|\Phi) \quad (14)$$

where

$$\mathcal{E}(\log M_{*,10}|\Phi) = 1 + erf \left( \alpha_M \frac{\log M_{*,10} - \mu_M}{\sqrt{2\sigma_M}} \right) \quad (15)$$

For the distribution of  $\Gamma_{*,10}$ , we use a Gaussian distribution to describe:

$$P(\Gamma_{*,10}|\Phi, \log M_{*,10}) = \frac{1}{\sqrt{2\pi\sigma_\Gamma^2}} \exp \left\{ -\frac{(\Gamma_{*,10} - \mu_\Gamma)^2}{2\sigma_\Gamma^2} \right\} \quad (16)$$

The relation between  $\log M_{*,10}$  and  $\Gamma_{*,10}$  is described by the  $\log M_{*,10}$  dependence on  $\mu - \Gamma$ :

$$\mu_\Gamma = \mu_{\Gamma,0} + \mu_{\Gamma,ms} (\log M_{*,10} - \log M_{*,10}^{pivot}) \quad (17)$$

Here we use a pivot value for  $\log M_{*,10}$ , which is the median value in each redshift bins.

Therefore, the full distribution of  $\Theta$  given  $\Phi$  is governed by the following set of hyperparameters:

$$\Phi = \{\mu_M, \sigma_M, \alpha_M, \mu_{\Gamma,0}, \mu_{\Gamma,ms}, \sigma_\Gamma\} \quad (18)$$

For the first part on the R.H.S. of Eq.12, we may rewrite it as

$$P(\mathbf{d}|\Phi) = P(\log M_{*,10}^{obs}|\log M_{*,10})P(\Gamma_{*,10}^{obs}|\Gamma_{*,10})P(z^{obs}|z) \quad (19)$$

Fortunately, according to Eq.1, Eq.8 and Eq.9, the uncertainty of  $\Gamma_{*,10}$  has cancelled out. In addition, as we use spectroscopic redshift, the uncertainty of  $z$  is negligible. Therefore, we only need to consider

**Table 2.** Bayesian hierarchical model fitting for the  $\Gamma_{*,10} - M_{*,10}$  relation in different redshift bins.

redshift	$\mu_M$	$\sigma_M$	$\alpha_M$	$\mu_{\Gamma,0}$	$\mu_{\Gamma,ms}$	$\sigma_{\Gamma}$
0.15-0.21	10.92	0.16	6.34	5.23	-0.34	0.10
0.21-0.28	10.94	0.15	4.34	5.73	-0.38	0.10
0.28-0.34	10.89	0.16	20.07	5.74	-0.38	0.10
0.34-0.40	10.89	0.15	2.09	4.03	-0.23	0.11

**Table 3.** Simulation parameters for different sets of simulation.

Set	$\xi$	$(M_h/M_*)_{\text{main}}$	$C_{\text{main}}$	$(r_s/R_{\text{eff}})_{\text{main}}$	$(M_h/M_*)_{\text{sat}}$	$C_{\text{sat}}$	$(r_s/R_{\text{eff}})$
D	1.0,0.5,0.2	49	8.0	11.6	49	8.0	11.6
D1	0.5	49	5.0	11.6	49	5.0	11.6
D2	0.5	49	8.0	6.0	49	8.0	6.0
D3	0.2	49	8.0	11.6	35	8.5	8.8
D4	0.2	49	8.0	11.6	75	8.0	15.0

the uncertainty of  $\log M_{*,10}$ , which we assume can be described by a Gaussian distribution:

$$P[\log(M_{*,10}^{\text{obs}}) | \log(M_{*,10})] = \frac{\mathcal{A}[\log(M_{*,10})]}{\sqrt{2\pi\sigma_{M_{*,10},\text{obs}}^2}} \exp\left\{-\frac{[\log(M_{*,10}) - \log(M_{*,10}^{\text{obs}})]^2}{2\sigma_{M_{*,10},\text{obs}}^2}\right\} \quad (20)$$

while  $\mathcal{A}[\log(M_{*,10})]$  satisfies

$$\int_{\log(M_{*,10,\text{min}})}^{\infty} d\log(M_{*,10}^{\text{obs}}) \frac{\mathcal{A}[\log(M_{*,10})]}{\sqrt{2\pi\sigma_{M_{*,10},\text{obs}}^2}} \exp\left\{-\frac{[\log(M_{*,10}) - \log(M_{*,10}^{\text{obs}})]^2}{2\sigma_{M_{*,10},\text{obs}}^2}\right\} = 1 \quad (21)$$

We sampled the posterior distribution of these hyperparameters and find the median value. The result is shown in Fig. 2. In addition, to illustrate the  $\Gamma_{*,10} - M_{*,10}$  relation, which is described by Eq. 17, we plot  $\mu_{\Gamma}$  as a function of  $\log M_{*,10}$  in Fig. 6, together with the median value of  $\mu_{\Gamma}$  in each mass bin.

### 3 SIMULATION

#### 3.1 Basic information

As mentioned in Sect. 1, we expect to understand how mergers, in particular, dry mergers with different merger mass ratio, would affect  $M_{*,10}$  and  $\Gamma_{*,10}$ . Therefore, we utilize a collection of 8 sets of dissipationless binary-merger simulations which has been used in Sonnenfeld et al. (2014) to construct a dry-merger model. These 8 sets of simulations have five different parameter settings and is reported in Table 3. Each set contains two runs of simulations with nearly identical parameter settings except for their different orbital angular momentum in order to take both 'head-on' and 'off-axis' encounter into consideration. All orbits are parabolic.

The two progenitors, i.e. main galaxy and satellite galaxy, in each set of simulation are spherical symmetric and are composed of dark matter halo and stellar component. The stellar profile can be described by  $\gamma$  model (Dehnen (1993); Tremaine et al. (1994))

$$\rho_{*}(r) = \frac{3-\gamma}{4\pi} \frac{M_{*,*}}{r^{\gamma}(r+r_*)^{4-\gamma}} \quad (22)$$

where  $M_{*}$  is the total stellar mass. The simulation adopt  $\gamma = 1.5$ .

The dark matter halo is described by NFW profile (Navarro et al. (1996))

$$\rho_{DM}(r) = \frac{M_{DM,0}}{r(r+r_s)^2} \exp\left[-\left(\frac{r}{r_{vir}}\right)^2\right] \quad (23)$$

According to Nipoti et al. (2009),  $r_s$  is the scale radius, while  $M_{DM,0}$  is a reference mass. A exponential cut-off is adopted as a truncation

of the halo, hence the total dark mass would not extend to infinity. As the summation of the two components, the total mass profile  $\rho(r) = \rho_{*}(r) + \rho_{DM}(r)$  is nearly isothermal: the slope  $\gamma'$  of the total mass profile in 8 sets of simulation lies in the range of  $1.97 \sim 2.03$ .

The simulation is run with FVFPS code (Fortran Version of Fast Poisson Solver, Londrillo et al. (2003); Nipoti et al. (2003)). The following code parameter values are adopted: minimum value of the opening parameter  $\theta_{min} = 0.5$  while the softening parameter  $\epsilon = 0.04R_{\text{eff}}$ , here  $R_{\text{eff}}$  represent the effective radius of the main galaxy. The timestep  $\Delta t$  is the same for all particles, while is allowed to vary depending on the maximum particle density  $\rho_{max}$  at that epoch. In particular, the timestep can be adapted by  $\Delta t = 0.3/(4\pi G\rho_{max})^{1/2}$ . The realisation of the initial condition is identical to that in Nipoti et al. (2009), with the mass of dark matter parts twice as heavy as stellar particles.

#### 3.2 Mock observation

In order to investigate the growth of these two parameters, we only need to focus on two snapshots of the simulation. The first snapshot is the initial state which contains the initial main galaxy and satellite galaxy, in fact, we only care about the main galaxy. The second snapshot is the final state when the merging process is finished leaving a remnant galaxy. The word 'finish' means that the remnant stellar system is relaxed and virialised, while the remnant galaxy is defined as the collection of dark matter particles and stellar particles that are bounded. We project the initial and remnant galaxies onto x-y plane so as to generate a mock observational image of these two, the mock image is shown in Fig. 4. The initial main galaxy is spherical, thus its image is a circle. In contrast, the remnant galaxy does not have this symmetry, hence we can observe that its image is an ellipse. In order to make a fair comparison, we then circularised the remnant ellipse. In particular, we measured the quadrupole moment of the remnant galaxy image, and then stretch and rotate the image according to this quadrupole moment until the image become a circle.

The next step we should do to generate a mock observation is to give a physical unit to the simulation data. In fact, the unit that Nipoti et al. (2009) use in the simulation, for instance, mass, length or velocity, do not have a physical meaning, they are just code units. Only after we specify a physical value for these 'code unit' can we calculate the  $M_{*,10}$  and  $\Gamma_{*,10}$  for our mock galaxies. We refer such operation as 'rescale' the simulation data. In order to understand what is the impact of mergers on the growth of  $M_{*,10}$  and  $\Gamma_{*,10}$ , we actually need a series of mock galaxies with different initial  $M_{*,10}$  and  $\Gamma_{*,10}$ . Therefore, we need to 'rescale' the simulation data several times to obtain that series of mock galaxies. Traditionally, changing the mass and length unit may affect the timestep used in the simulation, but as we only focus on two snapshots and ignoring the time that one merger event take, we believe this 'rescale' operation would not severely affect our result. If we set the length unit to  $1\text{kpc}$ , the effective radius of the main galaxy would be  $R_e = 1.22\text{kpc}$ . We then 'rescale' the simulation data accordingly, generated two additional set of mock galaxies with effective radius  $R_e = 7\text{kpc}$  and  $R_e = 12\text{kpc}$ . The reason for choosing these two specific value is explained in detail in Sect. 3.3. We show the evolution in  $M_{*,10}, \Gamma_{*,10}$  space in Fig. 5.

We can easily observe that for all three merger ratios, the parameter  $\Gamma_{*,10}$  always shows a decreasing trend, while for larger, more massive galaxies, the decrease in  $\Gamma_{*,10}$  tends to be more significant. On the other hand, the growth of parameter  $\log M_{*,10}$  is a bit more complicated. In general, the growth in  $\log M_{*,10}$  is always less than the growth in the total stellar mass  $\log M_{*}$ , which may indicating

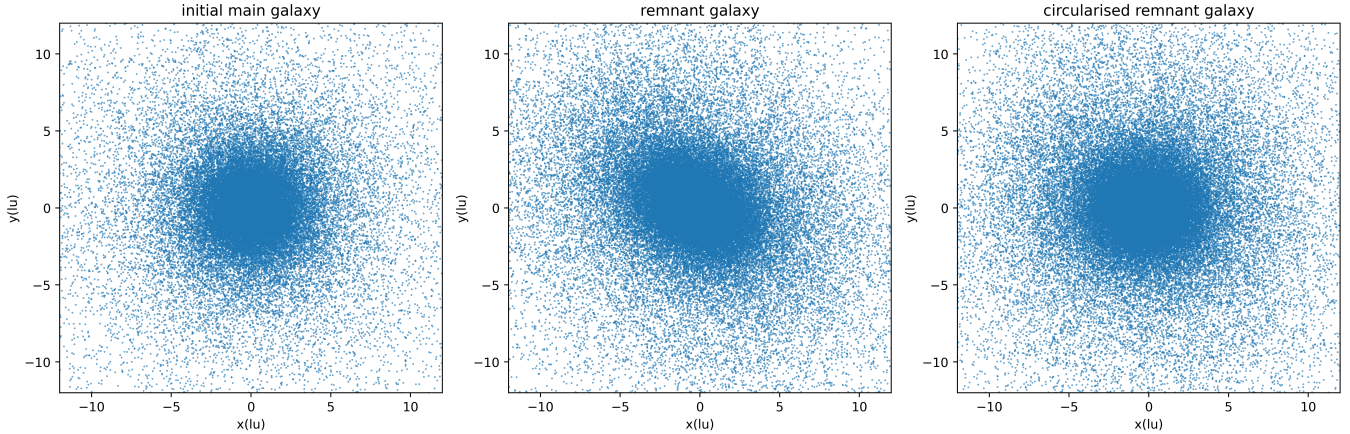


**Figure 4.** In this plot We choose the simulation set D3 to illustrate the mock images of main and remnant galaxies. The left panel shows the initial main galaxy, while the middle and right panels are the uncircularised and circularised remnant galaxy respectively. The unit is in code unit, instead of physical unit

that larger fraction of accreted mass are sunk in the outer region of the galaxy. In contrast with the  $\Gamma_{*,10}$ , smaller galaxies show a larger increase in  $\log M_{*,10}$ . Interestingly, if one pay more attention to the first two panels (top and middle panel), one can find that in some cases, the growth in  $\log M_{*,10}$  could be even negative after the merger. While for the largest merger ratio  $\xi = 1.0$  (bottom panel), the growth in  $\log M_{*,10}$  is always positive. The negative value informs us that the merger do varies the entire density profile of the galaxy, and the inner region of galaxies may experienced the most significant change comparing with the outer region. The impact on the inner region of galaxies tends to be stronger for mergers with smaller mass ratio. Small mass ratio minor-mergers may flatten the density profile, puffing-up the galaxies hence make  $\log M_{*,10}$  decrease and  $\log M_*$  increase simultaneously.

### 3.3 A toy model for the growth of $M_{*,10}$ - $\Gamma_{*,10}$ relation due to mergers

Firstly, in order to establish a toy model to predict the impact of mergers on the  $M_{*,10}$  -  $\Gamma_{*,10}$  relation, we need to know how many mass has galaxy grew during a certain period of time, or in other word, during a certain range of redshift. In our work, we adopted the result from [Moster et al. \(2018\)](#), which give a fitting formula of the fraction of stellar mass that accreted onto the main galaxy as a function of redshift for galaxies with different halo mass :

$$f_{acc}(z) = f_2 \exp[-f_1(z+1)] \quad (24)$$

For different halo mass, the parameter  $f_1$  and  $f_2$  are different, as shown in table 4. Here we only show the fitting parameter for two different, relatively large halo mass, as we only focus on the massive quiescent galaxies in our observation sample.

The next step is to estimate the stellar mass given the halo mass, hence we need the stellar-to-halo mass relation (SHM relation). This relation has a relatively large scatter, therefore inferring average halo mass from a given stellar mass is not equivalent to inferring the stellar mass from a given halo mass. In this work, we aim to know the average fraction of accreted mass, hence we need know what stellar mass correspond to a average halo mass  $10^{13} M_\odot$  (or  $10^{14} M_\odot$ ). We thus use Fig.4 in [Moster et al. \(2020\)](#) to operate a rough estimate on the stellar mass. For  $M_h = 10^{13} M_\odot$ , the stellar mass is about  $10^{11.1} M_\odot$ , while for  $M_h = 10^{14} M_\odot$ , the stellar mass is about  $10^{11.7} M_\odot$ . We then

**Table 4.** Simulation parameters for different sets of simulation.

$\log M_h$	$f_1$	$f_2$
13	1.09	0.55
14	0.94	1.43

make narrow stellar mass bins in our final sample, then calculated the median value of  $M_{*,10} : 10^{10.9} M_\odot$  and  $10^{11.4} M_\odot$  respectively.

Having estimate the  $M_{*,10}$ , we use the  $\Gamma_{*,10}$  -  $M_{*,10}$  relation of the highest redshift bin in Sect.4.2 to estimate the  $\Gamma_{*,10}$  for these two stellar mass. Then we try to 'rescale' our simulation data to let the 'rescaled' mock galaxy have a  $\Gamma_{*,10}$  that is close to the estimated value. The 'rescaled' mock galaxy correspond to halo mass  $M_h = 10^{13} M_\odot$  has a effective radius  $R_e = 7kpc$  with  $\Gamma_{*,10} \approx 1.57$ , while another mock galaxy has  $R_e = 12kpc$  with  $\Gamma_{*,10} \approx 1.39$ . We hope to explain the change of the  $M_{*,10}$  -  $\Gamma_{*,10}$  relation from the highest redshift bin to the lowest redshift bin using our toy model, hence we calculated the mass that has accreted to the galaxy during that range of redshift using Eq.24 and then translate the accreted mass fraction to the numbers of merger events with different merger ratio ( $\xi = 1.0, 0.5, 0.2$ ).  $\Delta M_{*,10}^{\text{total}}$  and  $\Delta \Gamma_{*,10}^{\text{total}}$  due to on entire merger event is already obtained and is shown in Fig.5, we thus estimate the growth of  $M_{*,10}$  and  $\Gamma_{*,10}$  by multiplying the number of mergers with the  $\Delta M_{*,10}^{\text{total}}$  and  $\Delta \Gamma_{*,10}^{\text{total}}$ .

## 4 RESULT

### 4.1 The growth of $M_{*,10}$ and $\Gamma_{*,10}$ in simulation

### 4.2 Observation result

Having investigate the result in simulations, we then operate the measurement to our observation sample. As a consequence of the completeness cut, galaxies with lower  $M_{*,10}$  value at higher redshift would be absent in our sample. To investigate the evolution trend in  $M_{*,10}$  -  $\Gamma_{*,10}$  relation, we have to either narrow the redshift range to include more low- $M_{*,10}$  galaxies or narrow the  $M_{*,10}$  range to include more high-redshift galaxies. In this work, we choose the latter one, meaning that we only focus on massive quiescent galaxies whose  $M_{*,10} \geq 10^{10.9} M_\odot$ . In addition, we set a lower limit on the redshift range  $z \geq 0.15$ . It's easy to observe some vertical stripe-like feature

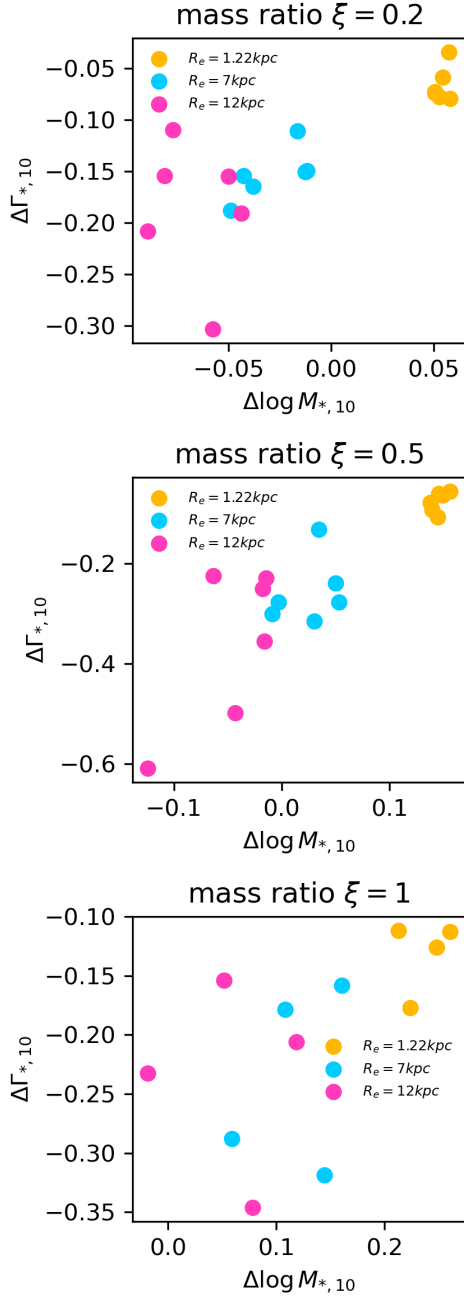


**Figure 5.** Three panels show the change in  $\log M_{*,10}$  and  $\Gamma_{*,10}$  due to mergers with three different merger ratio  $\xi$ , while the three colors represent different initial effective radius  $R_e$  of the main galaxy. The vertical dotted cyan line shows the logarithmic change in the total stellar mass for each merger ratio.

in Fig.3 at low redshift end, and is thought to be the effect of large scale structure by Driver et al. (2022). It is reasonable as the comoving volume at low redshift is relatively smaller, so it is more likely to suffer from cosmic variance. We thus determined this low-redshift cut in order to avoid such cosmic variance. The final sample we used to investigate the evolution is shown by cyan dots in Fig.3. We binned the sample in redshift and  $M_{*,10}$ , then calculated the median value of  $\Gamma_{*,10}$  in each bin. The  $\Gamma_{*,10}$  result is shown as a function of  $M_{*,10}$  in Fig.6 and as a function of redshift in Fig.7.

In Fig.6, we could observe an anti-correlation between  $M_{*,10}$  and

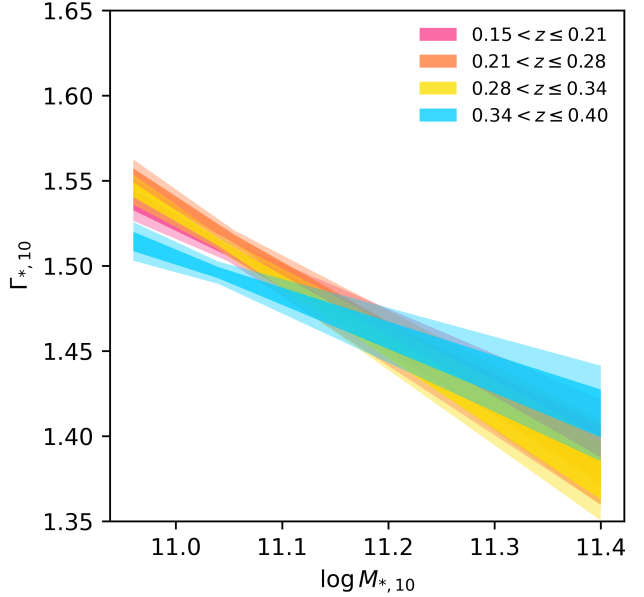


**Figure 6.** The  $M_{*,10} - \Gamma_{*,10}$  relation of our observation sample. The sample are divided into four redshift bins, and are shown in different colors. The error bar represents the standard error in each bins.

$\Gamma_{*,10}$ . Comparing the data in four redshift bins simultaneously, we can hardly see the evolution trend in this relation. In addition, if we focus on  $\Gamma_{*,10}$  only, as shown in Fig.7, we could reach a similar conclusion that there is no significant evolution in  $\Gamma_{*,10}$ . The  $\Gamma_{*,10}$  value in five different  $M_{*,10}$  are all almost constant as the redshift grows. The error bars in these two plots are standard error in each bin, i.e. the standard deviation divided by the square root of the number of galaxies in each bins. The error bar is relatively larger at higher  $M_{*,10}$  end, but it does not affect our conclusion as in Fig.6, the data points are still overlapping with each other in the same  $M_{*,10}$  bin and the  $\Gamma_{*,10} - z$  relation can still be reckoned as a horizontal line.

From the observation result shown in Fig.6 and Fig.7, we can hardly observe any evolution trend in  $M_{*,10} - \Gamma_{*,10}$  relation during the redshift range  $0.15 \leq z \leq 0.4$ . However, using observation data alone does not enable us to reach the conclusion that galaxies do not evolve at that period of time, cause various evolution scenarios may result in the lack of growth in  $M_{*,10} - \Gamma_{*,10}$  relation. For instance, if galaxy evolves along the  $M_{*,10} - \Gamma_{*,10}$  relation shown in Fig.6, then this relation would not show any growth in its intercept or slope and thus mimic the evolution trend. Nevertheless, taking the advantage of binary merger simulations, we are informed that how the  $M_{*,10}$  and  $\Gamma_{*,10}$  would evolve if the galaxies do experience mergers. The fact is, no matter what kind of merger one galaxy may experience, it would always leave a observable impact on the  $M_{*,10} - \Gamma_{*,10}$  relation. We may consider a idealized condition that every galaxy experienced a merger during the redshift interval  $0.4 \geq z \geq 0.15$  with mass ratio  $\xi = 0.2$ . From the upper panel of Fig.5 we can observe that this kind of merger will make massive galaxies goes down more rapid in  $M_{*,10} - \Gamma_{*,10}$  diagram than the less massive ones, which will drive this relation to be steeper. In addition, merger will increase  $M_{*,10}$  of less massive galaxies while decrease  $M_{*,10}$  of more massive ones, and thus twist the  $M_{*,10} - \Gamma_{*,10}$  relation in a clockwise direction, i.e. steeper the slope more intensively. However, we could not observe any evidence of such evolution trend in our observation sample. As

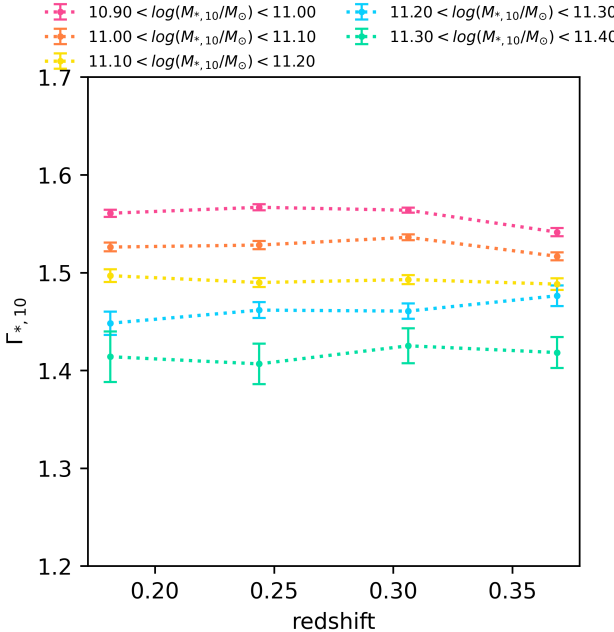


**Figure 7.**  $\Gamma_{*,10}$  as a function of redshift in each  $M_{*,10}$  bin. The sample are divided into five different  $M_{*,10}$  bins. The error bar represents the standard error in each bins.

is shown in Fig. 6, the slope of such relation in four different redshift bins can be considered as nearly identical. Therefore, we make our conclusion that galaxies do not experience significant growth due to mergers in the redshift range  $0.15 \leq z \leq 0.4$ .

## 5 DISCUSSION

### 5.1 Effect of spiral arms

The goal of our work is to investigate the evolution of quiescent galaxies without requiring the total flux of one galaxy. We expect all our galaxies can be perfectly described by a single Sérsic surface brightness profile, i.e. all galaxies are elliptical in shape. However, in reality, we only make a selection criteria based on the star-forming activities which is inferred from index  $Dn4000$ , hence we cannot exclude the potential risk of the contamination from spiral galaxies. Therefore, we need to know how spiral arms would affect the measurement of  $M_{*,10}$  and  $\Gamma_{*,10}$ .

Sonnenfeld (2022) performed a detailed analysis on the effect of spiral arms on the measurement of both total flux and the half-light radius  $R_e$ . Generally speaking, the existence of spiral arms would generate a bump in surface brightness near the light-weighted radius of the spiral arm. According to Fig. 6 of Sonnenfeld (2022), the best-fitting Sérsic model would begin to show a significant deviation from the real data at larger radii in respect to that "bump", while the inner region is not affected. This deviation would thus result in the bias in both total flux and  $R_e$ . In particular, the bias that introduced by spiral arm have a dependence on the ratio between the light-weight radius of spiral arm and the half-light radius of the galaxy. Both bias in total flux and  $R_e$  shows a increasing trend as this ratio grows while the ratio is smaller than about 1.8 and then decrease slightly as the ratio grows further, according to Fig. 7 in Sonnenfeld (2022).

In fact, one of the reason that we choose  $10\text{kpc}$  as the fixed aper-

ture is that this physical size is close to the average half-light radius of massive quiescent galaxies. Therefore, we can qualitatively conclude that the spiral arm of galaxies with similar size and mass of our sample will not leave a significant bias in our measurement. In one hand, if the spiral arm do affect the total flux and  $R_e$  significantly, then the light-weight radius of spiral arm has to be significantly larger than the half-light radius. However, the large size of the spiral arm also means the bump in surface brightness profile occurs at larger radii in respect to  $10\text{kpc}$ , making the  $10\text{kpc}$  as the unaffected inner region. On the other hand, if the aperture  $10\text{kpc}$  cannot be considered as the unaffected inner region, i.e. the light-weight radius of spiral arm is close to the half-light radius, then the total bias that introduce by spiral arm would be small, no matter the bias in  $M_{*,10}$  or  $\Gamma_{*,10}$ .

Although we believe that our work is not significantly biased by spiral arm, one still need to be careful when dealing with samples with smaller size. For instance, if the  $R_e \approx 5\text{kpc}$ , i.e.  $1.8 \times R_e \approx 10\text{kpc}$ , then the bias introduced by spiral arm will become significant, as the bias reaches its maximum while the bump also close to the  $10\text{kpc}$  aperture where we focus on. In this case, we may suggest to use a smaller aperture, for instance  $5\text{kpc}$ , to avoid the bias.

### 5.2 Limitations of our method

In this work, we adopted a new method that only focusing inside a fixed aperture  $10\text{kpc}$ , instead of attempting to obtain the entire light. Unlike the traditional parameter: effective radius  $R_e$  which is sensitive to different approaches of modeling the surface brightness profile, the fixed aperture in our method do not have such dependence. Therefore, we believe that our method provides a more robust way to make comparisons between simulations and observations and among different observations.

However, this robustness on the aperture size in turn placed a limitation on the sample selection. To ensure the aperture measurement is accurate, we need to obtain the spectrum of galaxies for a precise spectroscopic redshift measurement. Actually, our work is not affected by this requirement, as we also need the spectroscopic data to distinguish the quiescent galaxies from its star-forming counterparts. If we want to apply this method to a population of galaxies that do not rely on spectroscopic data to be selected, for instance, early type galaxies, then this spectroscopic data requirement would limit our sample to a relatively smaller range in both redshift and stellar mass. The work of Roy et al. (2018) could be a good example. They also use KiDs data, which is similar to ours, to investigate the evolution on the scaling relation of both early-type and late-type galaxies. Without the requirement of spectroscopic data, they use photometric redshift hence the sample could extend to higher redshift  $z \approx 0.6$  and lower total stellar mass  $M_* \approx 10^{11} M_\odot$  comparing to our sample, under the condition that they use KiDs DR2 data which has a significant smaller sample size than DR4.

To overcome this limitation, one may consider to use such surveys which cover a small field in the sky but could go to a deeper magnitude. For instance, using HSC (Utsumi et al. 2016) images combining with spectroscopic data from SHELS F2 (Geller et al. 2014) as Damjanov et al. (2019) did. SHELS F2 could reach 95% complete down to r-band magnitude  $r = 20.6$  in  $3.98 \text{ deg}^2$  area, roughly one magnitude deeper and covers about 55 times smaller region than GAMA. Nevertheless, the sample used in Damjanov et al. (2019) can still reach lower stellar mass limit  $M_* \approx 10^{10} M_\odot$ . However, the shortcoming of choosing deep and narrow field survey is that the sample size would be relatively small, which limit the precision of the measurement. In addition, the small field would also make the sample more sensitive to the cosmic variance. If one want to further anal-

use the number density of his sample, using such survey would be a bad choice. Hopefully, the incoming stage-IV survey could widen the survey coverage while deepen the survey limiting magnitude. We then thus do not need to make compromise between the coverage and the depth of the survey.

### 5.3 Number density of quiescent galaxies

In fact, to infer the growth mechanism that quiescent galaxies may undergo, the number density could provide some valuable information in addition to the evolution trend of  $M_{*,10} - \Gamma_{*,10}$  relation alone. For instance, [van Dokkum et al. \(2010\)](#) select galaxies with constant number density through different redshift bins, in order to select the same population of galaxies and therefore attained the growth of such population. Recently, [Bundy et al. \(2017\)](#) has studied the evolution in the number density of massive quiescent galaxies. Having considered a number of systematic that may affect the number densities, they claimed they did not detect a significant growth for these massive quiescent galaxies.

However, the most important thing in studying the number density is exactly the systematics. As the number of massive galaxies becomes less and less in high mass end, the number density becomes more and more sensitive to some potential systematics. Actually, as the narrow redshift and  $M_{*,10}$  range that we are focusing, our expectation is that the number density would not change significantly during this period of time. In order to reach the conclusion that the number density of massive quiescent galaxies stays constant during  $0.15 \leq z \leq 0.4$ , we need to be more careful about the systematics. To eliminate these systematic biases, we need to perform some detailed analysis on stellar mass estimation, the cosmic variance, for instance. Therefore, we leave the investigation on number density of massive quiescent galaxies in our sample to the future work.

## 6 CONCLUSION

In our work, we provide a new perspective to investigate the evolution of quiescent galaxies. Instead of trying to obtain the information of stellar mass and gravitational radius from the entire light of one galaxy, we switch our attention into the inner region. In particular, we focus on a fixed physical aperture  $10kpc$  and measure the mass and mass-weighted projected surface brightness slope  $\Gamma_{*,10}$  within. Although some information of the outer region is artificially ignored, these new parameterization could still provide us sufficient information to investigate the evolution of quiescent galaxies.

In order to understand what we can learn from the evolution of galaxies in  $M_{*,10}, \Gamma_{*,10}$  parameter space, we first utilize a collection of dissipationless binary merger simulations. We rescale each simulations to different size thus we could know if the size or mass would leave impact on the evolution in  $M_{*,10}, \Gamma_{*,10}$  parameter space. We divide the collection of simulations into three groups depending on their merger ratios  $\xi$ . In particular, we obtain the result for  $\xi = 0.2, 0.5$  and  $1.0$ . The result is shown in Fig.5. We conclude the result as follows:

- No matter what kind of merger one galaxy may experience, the density slope in the inner region, i.e.  $\Gamma_{*,10}$ , would always decrease after the merger. The decrease in  $\Gamma_{*,10}$  tends to be more significant for larger, more massive galaxies.
- The fraction growth of the mass enclosed in the inner region is always less than the fraction growth of the total stellar mass. That inform us that the mass growth via mergers is not homogeneous through galaxy, but prefer to sink in the outer region.

- For mergers with smaller mass ratio, especially for  $\xi = 0.2$ , the mass growth in the inner region would be negative for large galaxies, meaning that the density profile is flattened due to mergers.

Obtained the knowledge on how mergers will evolve galaxies in  $M_{*,10}, \Gamma_{*,10}$  space, we turn to observation data to investigate how do these two parameter grow in real world and attempting to infer the growth mechanism from the observational result. We select galaxies from GAMA survey and use KiDs r-band image to provide a Sérsic surface brightness fitting. We use a spectroscopic index  $D_n4000$  to distinguish quiescent galaxies from star-forming ones. In order to avoid bias introduced by the incompleteness of the sample, we define a redshift-dependent completeness cut on  $M_{*,10}$  and exclude those galaxies whose  $M_{*,10}$  is lower than this completeness limit, thus obtain the sample that are at least 95% complete in  $M_{*,10}$ . In addition, we further exclude some low redshift galaxies in consideration of cosmic variance. The final sample we utilized to investigate the evolution trend is shown in Fig.3 as cyan dots.

Using the Sérsic parameter provided by KiDs, in particular, using a CNN methods namely GalNet ([Li et al. \(2022\)](#)), we measured the  $M_{*,10}$  and  $\Gamma_{*,10}$  following the procedure that has been described in Sect.???. In addition, we operate a small modification to ensure the consistency between the stellar mass and Sérsic parameter. We then divide the sample into four redshift bins and five  $M_{*,10}$  bins, and calculate the median value of  $\Gamma_{*,10}$  in each bin. The result is shown in Fig.6 and Fig.7. We can tell from these two figures that neither the  $M_{*,10} - \Gamma_{*,10}$  relation nor the  $\Gamma_{*,10} - z$  relation shows a significant evolution trend. Having compared with the knowledge that we have obtained from simulations result, we conclude that galaxies with  $M_{*,10}$  larger than  $10^{10.9} M_\odot$  do not experience significant growth due to mergers in the redshift range  $0.15 \leq z \leq 0.4$ .

In conclusion, our work provide a robust way to make direct comparison between observation data and simulation result. Moreover, as the different behaviour of  $M_{*,10}$  and  $\Gamma_{*,10}$  during different mergers processes, our method also provide a new way to distinguish the growth mechanism of quiescent galaxies. At meanwhile, this method might have its limitation in studying less massive quiescent galaxies as our requirement of accurate physical aperture  $10kpc$  need the spectrum of galaxies to be measured, while the facilities of spectroscopic surveys limit our ability to detect fainter and more distant galaxies. As a consequence, although we have used the most advanced observational project GAMA and KiDs, we can only apply our method to galaxies with  $M_{*,10}$  no less than  $10^{10.9} M_\odot$  and redshift  $z$  lies between a relatively narrow range  $0.15 \leq z \leq 0.4$ . Fortunately, numbers of stage-IV surveys are under construction, e.g. CSST(China Space Station telescope, [Zhan \(2021\)](#)), Euclid ([Euclid Collaboration et al. \(2022\)](#)) and JWST(ADD CITE HERE). These surveys have stronger ability to detect fainter objects, thus could enrich the sample of quiescent galaxies and broaden the range of  $<_{*,10}$  and  $z$ . Hopefully, applying our method to these new data could provide us more detailed information on the growth of quiescent galaxies in a more robust way.

## REFERENCES

- Amaro V., et al., 2021, in Zelinka I., Brescia M., Baron D., eds., Vol. 39, Intelligent Astrophysics, pp 245–264, doi:10.1007/978-3-030-65867-0\_11
- Baldry I. K., et al., 2010, *MNRAS*, **404**, 86
- Balogh M. L., Morris S. L., Yee H. K. C., Carlberg R. G., Ellingson E., 1999, *ApJ*, **527**, 54
- Belli S., Newman A. B., Ellis R. S., 2015, *ApJ*, **799**, 206
- Bellstedt S., et al., 2020, *MNRAS*, **496**, 3235
- Bruzual G., Charlot S., 2003, *MNRAS*, **344**, 1000
- Bundy K., Leauthaud A., Saito S., Maraston C., Wake D. A., Thomas D., 2017, *ApJ*, **851**, 34
- Calzetti D., Armus L., Bohlin R. C., Kinney A. L., Koornneef J., Storchi-Bergmann T., 2000, *ApJ*, **533**, 682
- Carollo C. M., et al., 2013, *ApJ*, **773**, 112
- Chabrier G., 2003, *PASP*, **115**, 763
- D'Eugenio F., et al., 2023, Evolution in the Orbital Structure of Quiescent Galaxies from MAGPI, LEGA-C and SAMI Surveys: Direct Evidence for Merger-Driven Growth over the Last 7 Gy (arxiv:2303.05520)
- Daddi E., et al., 2005, *ApJ*, **626**, 680
- Damjanov I., Zahid H. J., Geller M. J., Utsumi Y., Sohn J., Souchereau H., 2019, *ApJ*, **872**, 91
- Dehnen W., 1993, *MNRAS*, **265**, 250
- Dekel A., Burkert A., 2014, *MNRAS*, **438**, 1870
- Dokkum P. G. v., Franx M., 1996, *MNRAS*, **281**, 985
- Driver S. P., et al., 2022, *MNRAS*, **513**, 439
- Eisenstein D. J., et al., 2023, arXiv e-prints, p. arXiv:2306.02465
- Euclid Collaboration et al., 2022, *A&A*, **662**, A112
- Fagioli M., Carollo C. M., Renzini A., Lilly S. J., Onodera M., Tacchella S., 2016, *ApJ*, **831**, 173
- Fan L., Lapi A., De Zotti G., Danese L., 2008, *ApJ*, **689**, L101
- Gardner J. P., et al., 2023, *PASP*, **135**, 068001
- Geller M. J., Hwang H. S., Fabricant D. G., Kurtz M. J., Dell'Antonio I. P., Zahid H. J., 2014, *VizieR Online Data Catalog*, p. J/ApJS/213/35
- Gordon Y. A., et al., 2017, *MNRAS*, **465**, 2671
- Hamadouche M. L., et al., 2022, *MNRAS*, **512**, 1262
- Hilz M., Naab T., Ostriker J. P., 2013, *MNRAS*, **429**, 2924
- Hopkins P. F., Bundy K., Hernquist L., Wuyts S., Cox T. J., 2010, *MNRAS*, **401**, 1099
- Hopkins A. M., et al., 2013, *MNRAS*, **430**, 2047
- Kauffmann G., et al., 2003, *MNRAS*, **341**, 33
- Kuijken K., et al., 2019, *A&A*, **625**, A2
- Li R., Napolitano N. R., Roy N., Tortora C., La Barbera F., Sonnenfeld A., Qiu C., Liu S., 2022, *ApJ*, **929**, 152
- Londrillo P., Nipoti C., Ciotti L., 2003, *Memorie della Societa Astronomica Italiana Supplementi*, **1**, 18
- Moster B. P., Naab T., White S. D. M., 2018, *MNRAS*, **477**, 1822
- Moster B. P., Naab T., White S. D. M., 2020, *MNRAS*, **499**, 4748
- Naab T., Johansson P. H., Ostriker J. P., 2009, *ApJ*, **699**, L178
- Navarro J. F., Frenk C. S., White S. D. M., 1996, *ApJ*, **462**, 563
- Newman A. B., Ellis R. S., Bundy K., Treu T., 2012, *ApJ*, **746**, 162
- Nipoti C., Londrillo P., Ciotti L., 2003, *MNRAS*, **342**, 501
- Nipoti C., Treu T., Bolton A. S., 2009, *ApJ*, **703**, 1531
- Oser L., Naab T., Ostriker J. P., Johansson P. H., 2011, *ApJ*, **744**, 63
- Roy N., et al., 2018, *MNRAS*, **480**, 1057
- Sonnenfeld A., 2020, *A&A*, **641**, A143
- Sonnenfeld A., 2022, *A&A*, **659**, A141
- Sonnenfeld A., Nipoti C., Treu T., 2014, *ApJ*, **786**, 89
- Suess K. A., et al., 2023, *ApJ*, **956**, L42
- Tal T., van Dokkum P. G., 2011, *ApJ*, **731**, 89
- Taylor E. N., et al., 2011, *MNRAS*, **418**, 1587
- Toft S., et al., 2007, *ApJ*, **671**, 285
- Tremaine S., Richstone D. O., Byun Y.-I., Dressler A., Faber S. M., Grillmair C., Kormendy J., Lauer T. R., 1994, *AJ*, **107**, 634
- Trujillo I., et al., 2006, *MNRAS*, **373**, L36
- Trujillo I., Conselice C. J., Bundy K., Cooper M. C., Eisenhardt P., Ellis R. S., 2007, *MNRAS*, **382**, 109
- Utsumi Y., et al., 2016, *ApJ*, **833**, 156
- Zhan H., 2021, *Chinese Science Bulletin*, **66**, 1290
- van Dokkum P. G., Brammer G., 2010, *ApJ*, **718**, L73
- van Dokkum P. G., Franx M., 2001, *ApJ*, **553**, 90
- van Dokkum P. G., et al., 2008, *ApJ*, **677**, L5
- van Dokkum P. G., et al., 2010, *ApJ*, **709**, 1018
- van der Wel A., et al., 2014, *ApJ*, **788**, 28

This paper has been typeset from a *TeX/LaTeX* file prepared by the author.